Asian Journal of Chemistry; Vol. 35, No. 3 (2023), 692-704

ASIAN JOURNAL OF CHEMISTRY

https://doi.org/10.14233/ajchem.2023.27288

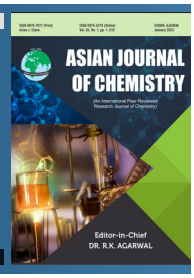

Fabrication of Eco-friendly UV-visible Driven Ni:$CaCO_3$ Photocatalyst for Sustainable Environmental Remediation

V. Ramasamy[1,*], T. Sathishpriya[1], E. Thenpandiyan[1] and G. Suresh[2]

[1]Department of Physics, Annamalai University, Annamalai Nagar-608002, India
[2]Department of Physics, Aarupadai Veedu Institute of Technology, Vinayaka Nagar, Paiyanur-603104, India

*Corresponding author: E-mail: srsaranram@rediffmail.com

Received: 11 December 2022; *Accepted*: 3 February 2023; *Published online*: 27 February 2023; AJC-21163

Nano $CaCO_3$, polymethyl methacrylate (PMMA) decorated Ni-doped $CaCO_3$ nanoparticles (CPN) were synthesized from natural calcium magnesium carbonate ($CaMg(CO_3)_2$) *via* biomimetic synthetic route. The obtained products were thoroughly characterized through various physico-chemical techniques such as UV-DRS, PL, FTIR, XRD, TG-DTA, FE-SEM with EDX mapping, HR-TEM and SAED patterns. The XRD results revealed that the prepared products were in pure rhombohedral structure with the size range of 20-50 nm, respectively. Compared to other synthesized products, the sample CPN_6 exhibited a blue-shifted band gap (2.7 eV) and red-shifted absorption and emission values. The morphological analysis of the samples shows the aggregated and rhombohedral with high porous like structure. The TG-DTA analysis shows the good thermal stability (up to 830 ºC). The photocatalytic activity exhibits a higher degradation efficiency 87% and 97% against methylene blue and rhodamine B dyes, respectively. The effect of different scavenger agents (ascorbic acid, $AgNO_3$, EDTA2NA and isopropanol acid) was used to examine the efficiency of the photocatalytic activity. Based on the results, the prepared CPN_6 nanoparticles show a great potential candidate for removal of organic dyes in the aqueous medium.

Keywords: Biomimetic synthesis, Dolomite rock, Calcite, Rhombohedral, Photocatalytic activity.

INTRODUCTION

Water is a fundamental need and plays a vital role in all form of life. Diverse water resources have been widely used due to the expansion of the urbanization and industrial activities [1,2]. Since wastewaters discharge from various industries, including textiles, dyeing, paper and food processing units, *etc*. was dumped directly into the river streams without being first treated, which became hazardous to plants and aquatic life [3,4]. As a result, this had a negative effect on the quality of the water. The main pollutants in freshwater resources are thought to be textile and other industrial dyes [5]. Convential wastewater treatment methods are ineffective against azo-based chromophores like methylene blue because of the covalent bonds formed between the reactive dyes. The decomposition or breakdown of dye into smaller, less harmful particles from bigger components is a problem and the subject of research for the scientific community worldwide.

The quality of water has recently been improved using a variety of chemical, biological and physical treatment techniques [6,7]. Although several physical treatment techniques like membrane filtration, adsorption, flocculation, *etc*. is a cost-effective process and does require routine maintenance [8]. The employment of several costly chemicals and the production of numerous byproducts are two drawbacks of the chemical process [9]. The application of enzymes and microorganisms in biological procedures has also been explored, despite the fact that these methods are not without their own challenges, including the need to scale up models for large-scale strategies [10,11]. The applications of photocatalysis in the air and water purification systems have received a considerable attention over the years. By exposing semiconductor materials to light, wastewater pollutants can be degraded in the photocatalytic process [12,13]. Semiconductor based photocatalysts have become increasingly popular all over the world as a result of the widespread recognition of the reduction-oxidation processes stimulated by light [14,15]. When carried out under normal conditions, no harmful byproducts are formed and also no adverse reaction conditions are required [16,17]. Photodegradation of variety of dyes, photocatalytic semiconducting materials such as titanates,

This is an open access journal, and articles are distributed under the terms of the Attribution 4.0 International (CC BY 4.0) License. This license lets others distribute, remix, tweak, and build upon your work, even commercially, as long as they credit the author for the original creation. You must give appropriate credit, provide a link to the license, and indicate if changes were made.

perovskite oxides of Ca/Ti/Cu/Fe/Co/Zn/Ni, sulphides of Cd/Zn and heterogeneous of carbon nanotubes/graphene have been widely used [18,19]. The $CaCO_3$ substance was utilized in the recent works. It is significant that $CaCO_3$ support can deliver important chemical species (such as CO_3^{2-}, HCO_3^- and OH^-) in aqueous solution, when combined with OH^-, can produce carbonate radicals or CO_3^{2-} and thus assist in the breakdown of organic compounds and microorganisms [20,21]. The steady-state concentration of CO_3^{2-} has been calculated to be two orders of magnitude greater than the steady-state concentration of $^{\bullet}OH^-$. Therefore, it is important to develop a substance and investigate the crucial role that $^{\bullet}CO_3^-$ plays in minimizing the permanence of different organic pollutants in wastewater [22].

One of the carbonate minerals, $CaMg(CO_3)_2$ (dolomite), was used in this study to prepare $CaCO_3$ [23]. Calcium and magnesium are the main components, with varying amounts of other elements (Na, Cu, Fe, and Sr) and compounds (SiO_2) present [24]. There are several reports available from various biominerals and biowastes to synthesize $CaCO_3$, but extraction of $CaCO_3$ from $CaMg(CO_3)_2$ (dolomite) rock is rarely reported. For the synthesis of $CaCO_3$ nanoparticles in the photocatalyst activity, it is crucial to control the particle size, polymorphism and shape of the desired material [25]. The addition of suitable organic polymers and surfactants makes this possible, since they also offer resistance to ultraviolet radiation, stability, chemical inertness, high durability and ease of availability [26]. The polymers further enhance the photocatalytic activity of the materials by facilitating the adsorption of the target organic dye molecules on their surfaces [27].

Doping of suitable semiconductors can boost the photocatalytic activity and doped photocatalysts frequently exhibit superior activity [28]. Wide bandgap semiconductors produced from metal oxide-based nanomaterials are well-controlled structural, crystallographic and high surface area. Additionally, they exhibit advantageous traits such as non-toxicity and high water stability [29]. In photocatalytic applications, doped $CaCO_3$ is crucial to alter the optical response of the semiconductor photocatalyst [30]. The various synthesis method used so far in synthesize $CaCO_3$ nanoparticles are co-precipitation [31], hydrothermal [32], sol-gel, low temperature microwave solid state synthesis [33], micromulsion [34] and mechanochemical processing [35], *etc*. In the present work, photodegradation of organic dyes such as methylene blue and rhodmine B were investigated using nano $CaCO_3$ and nickel doped with PMMA template $CaCO_3$ nanoparticles synthesized by biomimetic method.

EXPERIMENTAL

The chemicals *viz*. anhydrous sodium carbonate, sucrose, polymethyl methacrylate (PMMA), isopropanol acid (IPA), $NiCl_2$, $AgNO_3$, ascorbic acid (AA), EDTA2Na, rhodamine B and methylene blue were obtained from Sigma-Aldrich, USA. All compounds were of analytical grade with 99.9% pure. The glasswares used in this experiment were cleaned with dil. HNO_3 acid and then dried prior to use. The preparation of the samples and all dilutions were done with ultrapure water.

Natural dolomite rock: High-grade crystalline natural $CaMg(CO_3)_2$ (dolomite) samples were obtained from Manur, India at coordinates 8.8550ºN latitude and 77.6522ºE longitude. To eliminate the organic debris and other contaminants, the samples were often exposed to a variety of pretreatments, for which dil. HCl was utilized.

Preparation of calcium sucrate solution: Ball mills were used to crush and grind the samples. An ASTM 230 (62.5 µm) screen sieve was used for the filtration. To get CaO·MgO, the powdered sample was heated in a muffle furnace for 2 h at 900 ºC. Then, 100 mL of 1 M sucrose solution containing 10 g of CaO·MgO powder was added and the mixture was rapidly agitated for 1 h at room temperature. To collect soluble calcium sucrose solution, the solution was filtered using suction.

Synthesis of nano $CaCO_3$ (with and without polymer) and $CaCO_3$/PMMA:Ni nanoparticles: To obtain nano PCC (precipitate calcium carbonate) without polymer, the obtained calcium sucrate solution was added to 80 mL of 1 M $NaCl_2$ solution in a 500 mL flask. The solution was rapidly agitated and heated to 80 ºC for 2 h. The same process was used to get the PMMA mediated $CaCO_3$ nanocomposite by adding 10 mL of 1 M PMMA dropwise into the calcium sucrate solution. For the preparation of $CaCO_3$/PMMA:Ni nanoparticles, added 10 mL of (0.02 M, 0.04 M, 0.06 M, 0.08 M, 0.10 M and 0.12 M) $NiCl_2$ (CPN_1-CPN_6) dropwise to $CaCO_3$/PMMA solution. The obtain product was cleaned with distilled water three or four times before being dried at 100 ºC in a hot air oven.

Characterization: The FTIR spectra were recorded using a SHIMADZU-8400 in transmittance mode at a resolution of ± 4 cm^{-1} using KBr pellet in the 4000-400 cm^{-1} range. The XRD patterns of the powder samples were obtained using an Intel Equinox-1000 diffractometer in the 2θ range from 10º to 70º. The samples were recorded at room temperature having a Cu*K*α radiation source (λ = 1.5406 Å) and a scanning speed of 0.02/s. The Simultaneous Thermal Analyzer (NETZSCH-STA-449F3-JUPITER) was used to thermal stability (TG-DTA) at a heating rate of 10 ºC/min in a nitrogen gas atmosphere. The morphological examinations and elemental analyses of the products were taken using a CARL ZEISS-SIGMA 300 FE-SEM microscope equipped with EDX. The particle size and SAED patterns were obtained using a Tecnai G^2 20 S-TWIN TEM instrument with a working voltage of 20 to 200 kV and a HRTEM (point and a line resolution is 0.24 and 0.14 nm). The UV-VIS-DRS spectra were recorded using a UV-VIS-NIR spectrometer linked with an ISR- 603 integrating sphere unit and operating between 200 and 800 nm. The photoluminescence spectra of the prepared samples were analyzed using a Horiba Jobin Yvon Fluoromax-4 spectrofluorometer. The Shimadzu-UV 1800, UV-VIS spectrophotometer was used to record the optical absorption spectra of the samples in the wavelength range 200-800 nm.

RESULTS AND DISCUSSION

Optical properties

UV-Vis-DRS analysis: The UV-vis-DRS analysis was used to study the optical properties of natural dolomite, pure

nano $CaCO_3$ and $CaCO_3$/PMMA nanoparticles. As shown in Fig. 1a, dolomite has four weak absorption peaks. However, nano $CaCO_3$ synthesized from natural $CaMg(CO_3)_2$ (dolomite) (Fig. 1b) and $CaCO_3$/PMMA nanoparticles exhibit substantial UV absorption in the 270-350 nm range and a poor absorption in the 220-270 nm range. The presence of two absorption peaks in the nano $CaCO_3$ (262 and 305 nm) and $CaCO_3$/PMMA (303 and 318 nm) nanoparticles indicated that the samples are free of impurities [36]. The elimination of two additional peaks (319 and 375 nm) during the synthesis of nano $CaCO_3$ and $CaCO_3$/PMMA nanoparticles may be attributable to the absence of contaminants from natural dolomite. When compared to nano $CaCO_3$ (without polymer) (262 nm), the peak at 261 nm has the highest absorption in $CaCO_3$/PMMA nanoparticles, which is due to the blue-shift. However, the encapsulation of PMMA on the nano $CaCO_3$ has led to an increase in intensity in $CaCO_3$/PMMA nanoparticles (261 nm) and decrease in crystallite size, which may be caused by quantum confinement effect [37].

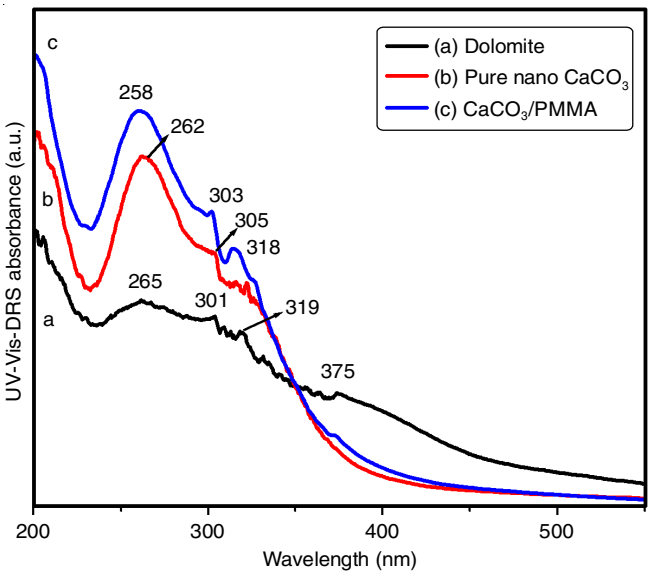

Fig. 1. UV-Vis-DRS absorption spectra of (a) dolomite rock, (b) pure nano $CaCO_3$ (without polymer) and (c) $CaCO_3$/PMMA

Fig. 2a-f indicates the UV-Vis-DRS analysis of the synthesized $CaCO_3$/PMMA:Ni nanoparticles. The absorbance peaks of CPN_1, CPN_2, CPN_3, CPN_4, CPN_5 and CPN_6 were observed at 262, 259, 257, 260, 261 and 263 nm, respectively. The CPN_6 (263 nm) exhibited the highest absorption and red-shift when compare with other samples. The influence of Ni doping on absorption behaviour is clearly observed. It demonstrates that the extremely wide absorption band may be attributable to the *d-d* transition of Ni ion from the ground to an excited state, which is likely cause the structural deformation and the emergence of vacancy, resulting in an impurity state in the core lattice. This impurity state can narrow the band gap, enhance the absorption and also creating a lattice distortion and defect energy level in the particles during the preparation process [38].

The optical band gap was determined using the absorbance which follows the electron excitation from the conduction band to the valence band. To explore the optical transitions, several

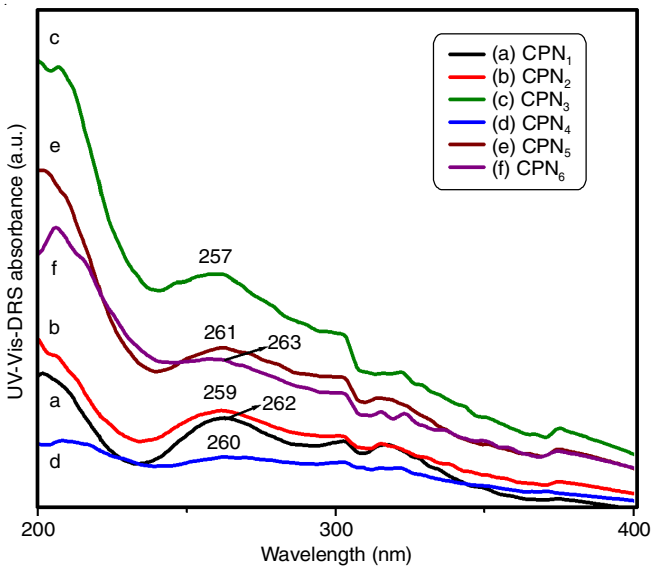

Fig. 2. UV-Vis-DRS absorption spectra of various concentrations of Ni:$CaCO_3$/PMMA

approximations must be shown while getting the normal energy scaling assurance for direct and indirect transitions. The absorption coefficient F(R) was calculated using Kubelka-Munk (K-M) function (eqn. 1):

$$F(R) = \frac{(1-R)^2}{2R} = \frac{\alpha}{S} \quad (1)$$

where R = Reflectance of an infinitely thick samples, α and S is the Absorption and scattering coefficient. The band edge absorption energy (E_g) is given by eqn. 2:

$$\alpha = A(E - E_g)^n \quad (2)$$

E_g is calculated using eqn. 3:

$$E = h\nu; \nu = \frac{c}{\lambda} E_g = \frac{1240}{\lambda} eV \quad (3)$$

where, A is a constant, λ is the absorption wavelength.

The direct band gap values of nano $CaCO_3$, CPN_1, CPN_2, CPN_3, CPN_4, CPN_5 and CPN_6 nanoparticles were found be 2.77, 2.95, 2.90, 3.0, 2.85, 2.8 and 2.7 eV, respectively, as calculated from the Tauc plots (Fig. 3a-g). The band gap value (2.7 eV) of CPN_6 nanoparticles is lower than that of other synthesized products [39]. According to Zidan & Abu-Elnader [40], the addition of PMMA to the $CaCO_3$ matrix may result in the localized state of multiple colour centers overlapping with the higher wavelength absorption, indicating a decrease in the energy band gap.

Photoluminescence studies: Fig. 4a-c displays the photoluminescence (PL) spectra for natural dolomite, pure nano $CaCO_3$ (with & without polymer) were recorded at room temperature. The natural dolomite, pure nano $CaCO_3$ and $CaCO_3$/PMMA nanoparticles exhibits the emission peak at 465, 460 and 454 nm, respectively. The $CaCO_3$/PMMA emission peak is (454 nm) blue-shifted compared to pure nano $CaCO_3$ (460 nm).

From Fig. 5a-f, the emission peak of CPN_1, CPN_2, CPN_3, CPN_4, CPN_5 and CPN_6 nanoparticles exhibited at 461, 462, 458, 463, 464 and 466 nm, respectively. This demonstrates that

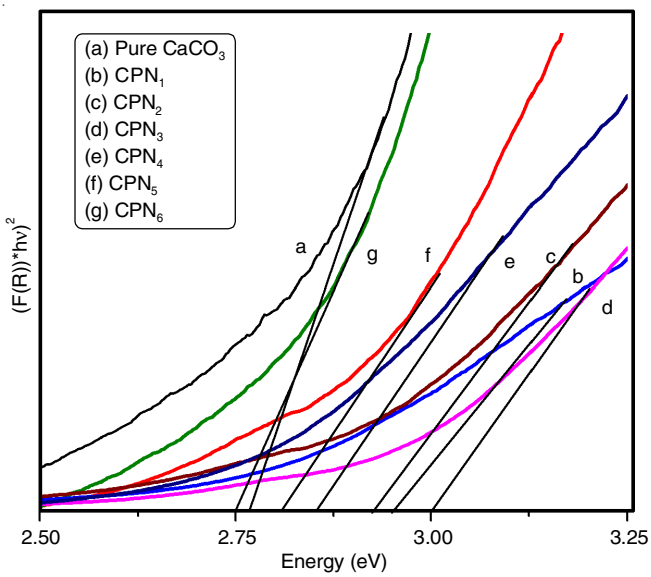

Fig. 3. Direct band gap energy spectra of pure nano $CaCO_3$ (without polymer) and various concentrations of Ni:$CaCO_3$/PMMA

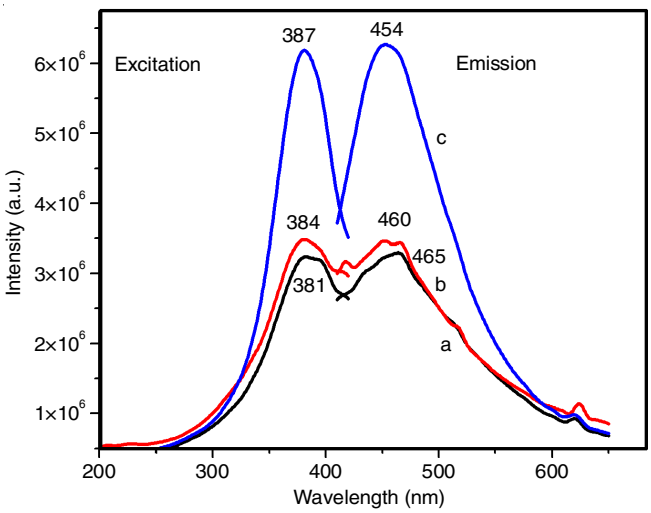

Fig. 4. PL spectra of (a) natural dolomite, (b) pure nano $CaCO_3$ (without polymer) and (c) $CaCO_3$/PMMA

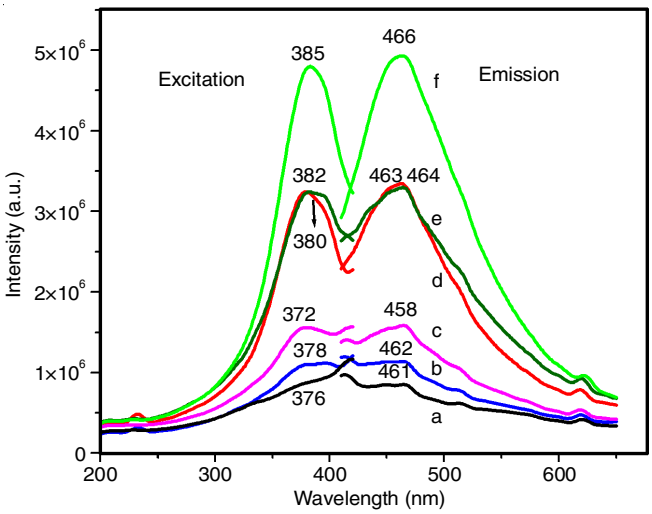

Fig. 5. PL spectra of various concentrations of Ni:$CaCO_3$/PMMA

when compared to CPN_3 nanoparticles, the band gap energy of other samples was lowered. On the other hand, the observed emission is only due to the defects. Excess oxygen ions in the crystal creat the defect centers and are present at the level of trapping. When the electron is excited by light radiation, the electron-hole recombination process allows for the observation of the PL emission. The particle size of CPN_3 nanoparticles was less than that of other synthesized products, indicating less crystallization. As a result, the PL intensity increased rapidly with decreasing size. The CPN_3 nanoparticles are blue shifted (458 nm), while the CPN_1 and CPN_6 nanoparticles are red shifted compared with other synthesized products. Based on the UV-DRS and PL results, three samples (CPN_1, CPN_3 and CPN_6) were chosen for further analysis.

FTIR studies: The spectrum (Fig. 6a) obtained for natural dolomite displays the CO_3^{2-} absorption peaks at about 1431 cm^{-1} (ν_3), 880 cm^{-1} (ν_2), and 728 cm^{-1} (ν_4), as well as minor absorption peaks around 2530 and 1819 cm^{-1}. These peaks indicate the carbonate ion's common distinctive feature in the sample [41]. The appearance of another frequency at 3694 cm^{-1} is due to the characteristic peak of $Al_2O_3{\cdot}2SiO_2{\cdot}2H_2O$ (kaolinite). The presence of quartz (SiO_2) crystals in the sample is indicated by the low-intensity weak peak at 1089 cm^{-1} [42].

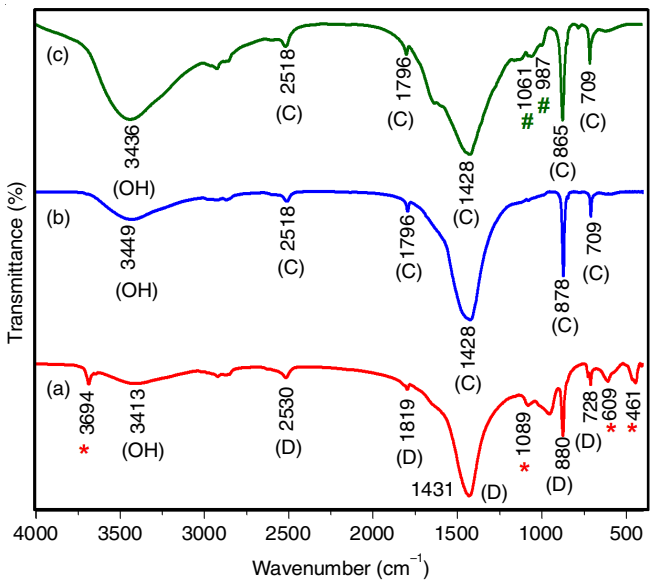

Fig. 6. FTIR spectrum of (a) natural Dolomite, (b) pure nano $CaCO_3$ (without polymer) and (c) $CaCO_3$/PMMA

Fig. 6b depicts the FTIR spectrum of synthesized pure $CaCO_3$ nanoparticles (without polymer). It shows the presence of carbonate peaks at 709, 878, 1428, 1796 and 2518 cm^{-1} in the calcite form. The FTIR spectrum of PMMA coated $CaCO_3$ (Fig. 6c) shows the presence of all major and minor $CaCO_3$ (calcite) peaks and are well-matched with $CaCO_3$ in their pure form. The occurrence of peaks at 1061 and 987 cm^{-1} depicts the presence of PMMA on the surface of product [43,44]. The impact of PMMA on $CaCO_3$ was also seen in the widening of the specific absorption peak at 1429 cm^{-1} (ν_3) [43]. A common peak at around 3413, 3449 and 3436 cm^{-1} are due to adsorbed –OH stretching in all the samples [37].

Fig. 7a-c shows that FTIR spectra of synthesized CPN_1, CPN_3 and CPN_6 nanoparticles. Most of the absorption bands observed in the synthesized products represent the presence of pure nano $CaCO_3$, however the presence of one additional peak at 1105 cm^{-1} may be due to the influence of PMMA on the surface of $CaCO_3$. Moreover, the appearance of a peak at around 400 cm^{-1} shows the presence of Ni in the $CaCO_3$ matrix [45]. As the concentration of Ni increases, all the peaks were braded when compared with the nano $CaCO_3$, which confirmed that more Ni ions are incorporated in the $CaCO_3$ matrix [37].

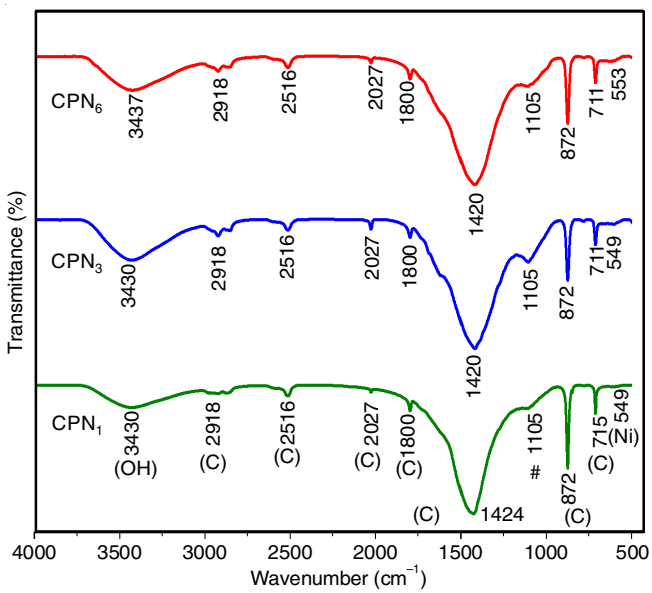

Fig. 7. FTIR spectrum of (a) CPN_1, (b) CPN_3 and (c) CPN_6

XRD studies: Fig. 8a-c demonstrates the crystalline nature and phase composition of the samples. The XRD pattern of natural dolomite (Fig. 8a) indicates the nine planes at 2θ value 23.98º, 30.98º, 33.41º, 36.40º, 41.01º, 44.89º, 50.49º, 51.06º and 64.31º with corresponding (*hkl*) values of (012), (104), (006), (110), (113), (202), (108), (116) and (208), respectively. The diffraction planes were well-matched with JCPDS file 84-1208 and confirmed the crystallinity of dolomite [37]. Additionally, three planes were also observed at 2θ values of 29.41º, 47.37º and 48.46º showing the presence of accessory minerals (quartz SiO_2) and orthoclase feldspar ($KAlSi_3O_8$) in a raw sample. These peaks values were also matched with JCPDS files 87-1247 and 89-8572. Simiarly, Fig. 8b shows XRD patterns of synthesized $CaCO_3$ and exhibit the characteristic planes at 22.67º, 29.11º, 31.08º, 35.56º, 39.01º, 42.75º, 47.22º, 48.25º, 56.19º, 57.04º, 60.21º and 64.22º with (*hkl*) values of (012) (104), (006), (110), (113), (202), (018), (116), (211), (122), (119) and (300), respectively. These planes were also well-matched with the calcite polymorph of $CaCO_3$ with rhombohedral structure (JCPDS file No: 86-2342) [37,46].

From Fig. 8c, the presence of all the characteristic planes were well-matched with the pure nano $CaCO_3$. The characteristic plane at 2θ (29.02º) with plane (104) in $CaCO_3$/PMMA is slightly shifted to lower angle side when compared with pure nano $CaCO_3$ (2θ = 29.11º). This is due to the influence of polymer (PMMA) on the surface of the product. No other

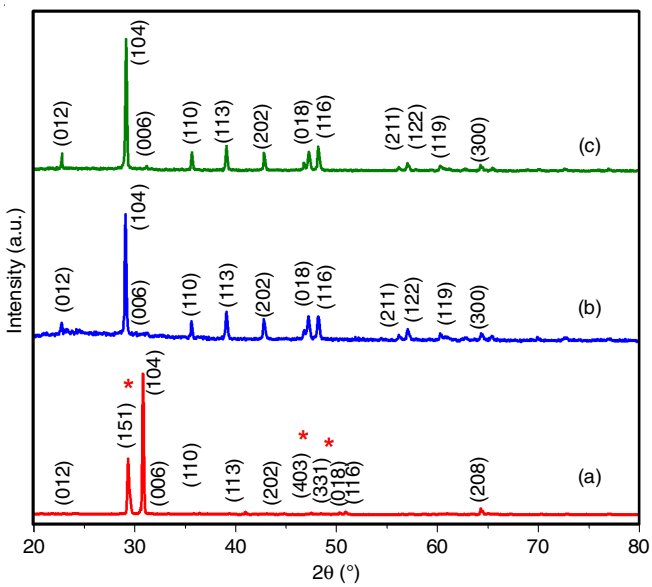

Fig. 8. XRD pattern of (a) natural dolomite, (b) pure nano $CaCO_3$ (without polymer) and (c) $CaCO_3$/PMMA

additional peaks were observed in the samples. These results are consistent with the FTIR analysis. The Scherrer's formula (eqn. 4) was used to calculate the average crystallite size of $CaCO_3$ and $CaCO_3$/PMMA.

$$D = \frac{k\lambda}{\beta\cos\theta}(Å) \quad (4)$$

where D = crystallite size (nm), k = constant (0.94), θ = diffracted angle and β = full width half maximum. The calculated average crystallite size of $CaCO_3$ and $CaCO_3$/PMMA were found to be 48 and 34 nm, respectively.

Fig. 9a-c depicts the XRD patterns of CPN_1, CPN_3 and CPN_6 nanoparticles. All the diffraction planes are well matched with the pure nano $CaCO_3$ and no other secondary plane were obse-

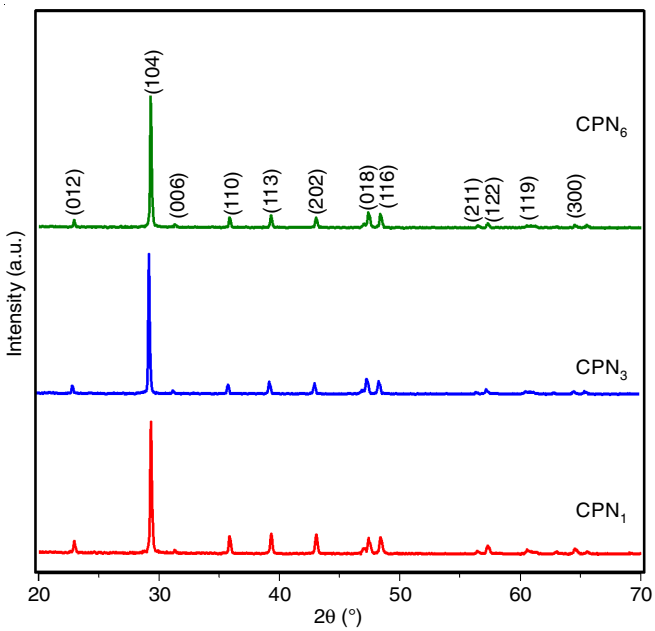

Fig. 9. XRD pattern of (a) CPN_1, (b) CPN_3 and (c) CPN_6

rved. However, an increase of dopant concentration increases the FWHM (broadening) of all the planes and decreases the peak intensity. Table-1 shows the calculated average crystal size of CPN_1, CPN_3 and CPN_6 nanoparticles which were 30, 24 and 37 nm, respectively. The calculated average crystallite size clearly indicates that an increase of Ni ions concentration gradually decreases the crystallite size. It could be attributed due to the incorporation of Ni ions in the $CaCO_3$ lattice. Gradual decreases in crystallite size may be happened as Ni ions have an ionic radius of 0.12 Å which is smaller, compared to the ionic radius of Ca^{2+} ions (1.14 Å). Also, this may be due to the secretion of the doping ions at the grain boundary and prevent the growth of nanocrystallite in the nanoparticles [47].

As a result of the aforementioned phenomenon, several lattice characteristics, strain and dislocation density may shift. Hence, the average dislocation density and average microstrain were calculated using eqns. 5 and 6 [48,49]. In addition to the crystallite domain size, the microstrain-induced lattice distortion also contributes to the XRD peak broadening [50].

$$\varepsilon = \frac{\beta \cos\theta}{4} \quad (5)$$

$$\delta = \frac{1}{D^2} \quad (6)$$

where β is the FWHM, θ is the Bragg's angles and D is the particle size (nm). According to the calculated values (Table-1), the structural parameter values were increased as the crystallite size decreases. The larger dislocation density implies a greater hardness. When strain increases, dislocation density rises while grain size is reduced. Above a particular grain size limit (20 nm), the strength of materials improves in lower grain size [51,52].

According to the estimated values, the crystallite size decreases when dislocation density increases. In present work, sample CPN_6 possesses the best beneficial features such as high crystallite sizes, low dislocation density and microstrain owing to the loss of many oxygen atoms when all computed values are compared. This demonstrates that Ni ions have a strong impact on the crystal lattice. These were ascribed to an increase in Ca concentration, which enhanced the pinning effect of Ca atoms on the density of edge dislocations. Since the current work focused on the photocatalytic applications, the higher crystal size sample CPN_6 is chosen for further investigation for the photocatalytic activity.

Williamson-Hall plot: The Williamson-Hall plot of pure nano $CaCO_3$, PMMA mediated $CaCO_3$, CPN_1, CPN_3 and CPN_6 nanoparticle is shown in Fig. 10a-e. The crystallite sizes of the products are also computed from the Williamson-Hall plot. The calculated crystallite values using the Scherrer's equation and the Williamson-Hall plot are nearly identical (Table-1).

Thermal analysis: TG-DTA thermograms of dolomite rock, pure nano $CaCO_3$ and CPN_6 nanoparticles are shown in Fig. 11a-c. A single decomposition peak was observed (Fig. 11a) in natural dolomite. It has a mass loss of 47.76% from room temperature to 841 ºC due to the thermal dissociation of dolomite to CaO·MgO [53]. The DTA curve of natural dolomite indicates the endothermic peak at 841 ºC.

In case of pure nano $CaCO_3$ and CPN_6 nanoparticles, the thermograms (Fig. 11b-c) reveals two mass losses. The initial mass loss occurs from room temperature to 299 ºC (4.55%,pure nano $CaCO_3$) and about 3.25% from room temperature to 325 ºC (CPN_6), which is due to the dehydration and physically adsorbed moisture or organic component removal [54]. The removal of

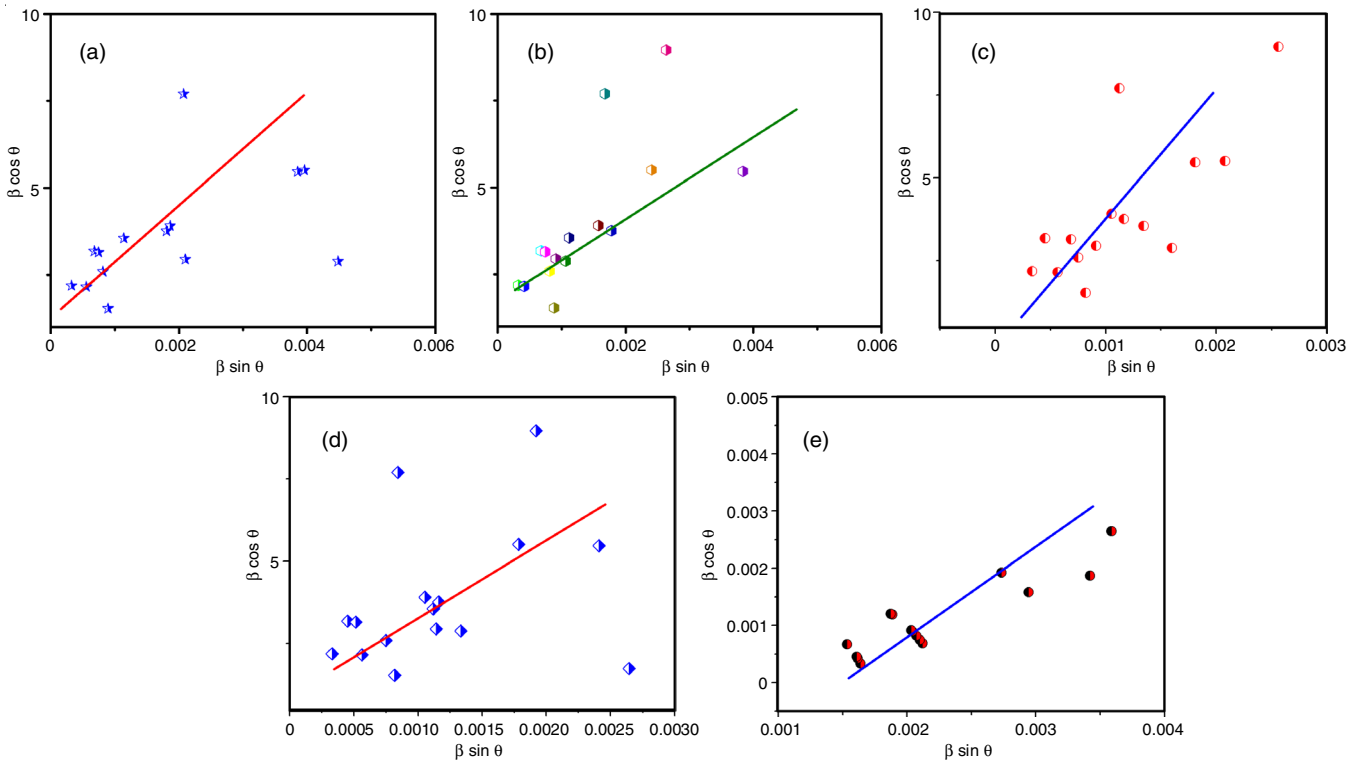

Fig. 10. W-H plots of (a) pure nano $CaCO_3$ (without polymer), (b) $CaCO_3$/PMMA, (c) CPN_1, (d) CPN_3 and (e) CPN_6

TABLE-1
XRD PARAMETERS OF NANO $CaCO_3$, $CaCO_3$/PMMA, CPN_1, CPN_3 AND CPN_6

Samples	Lattice parameters (Å)		Average dislocation density (δ) × 10^{14}	Average microstrain (ε) × 10^{-3}	Average crystallite size (nm)	
	a	c			Scherrer formula	W-H plot
Pure nano $CaCO_3$	2.52200	17.3247	41.77	1.04	48	49
$CaCO_3$/PMMAA	2.51730	17.1192	48.96	1.19	34	35
CPN_1	2.50390	17.2518	92.55	1.37	30	31
CPN_3	2.50170	17.3347	98.17	1.69	24	25
CPN_6	2.50373	17.3240	85.18	1.17	37	38

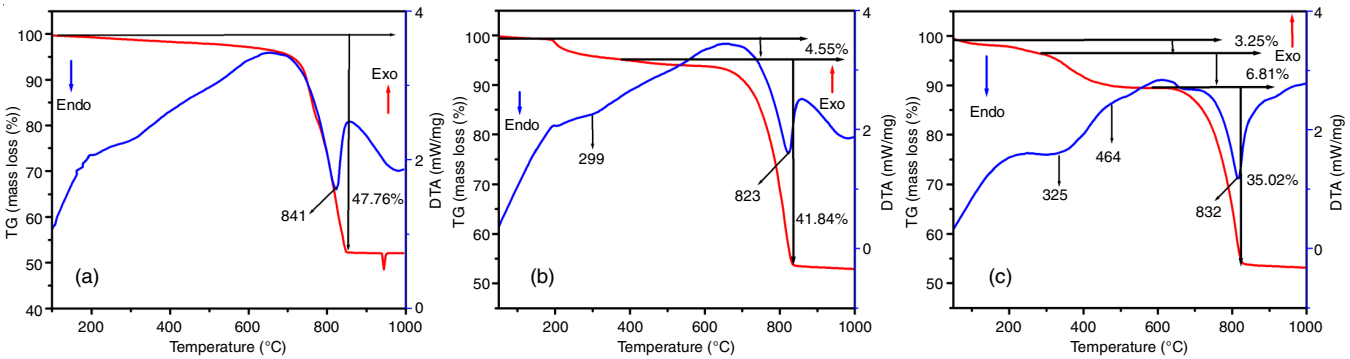

Fig. 11. TG-DTA curves of (a) natural dolomite, (b) pure nano $CaCO_3$ (without polymer) and (c) CPN_6

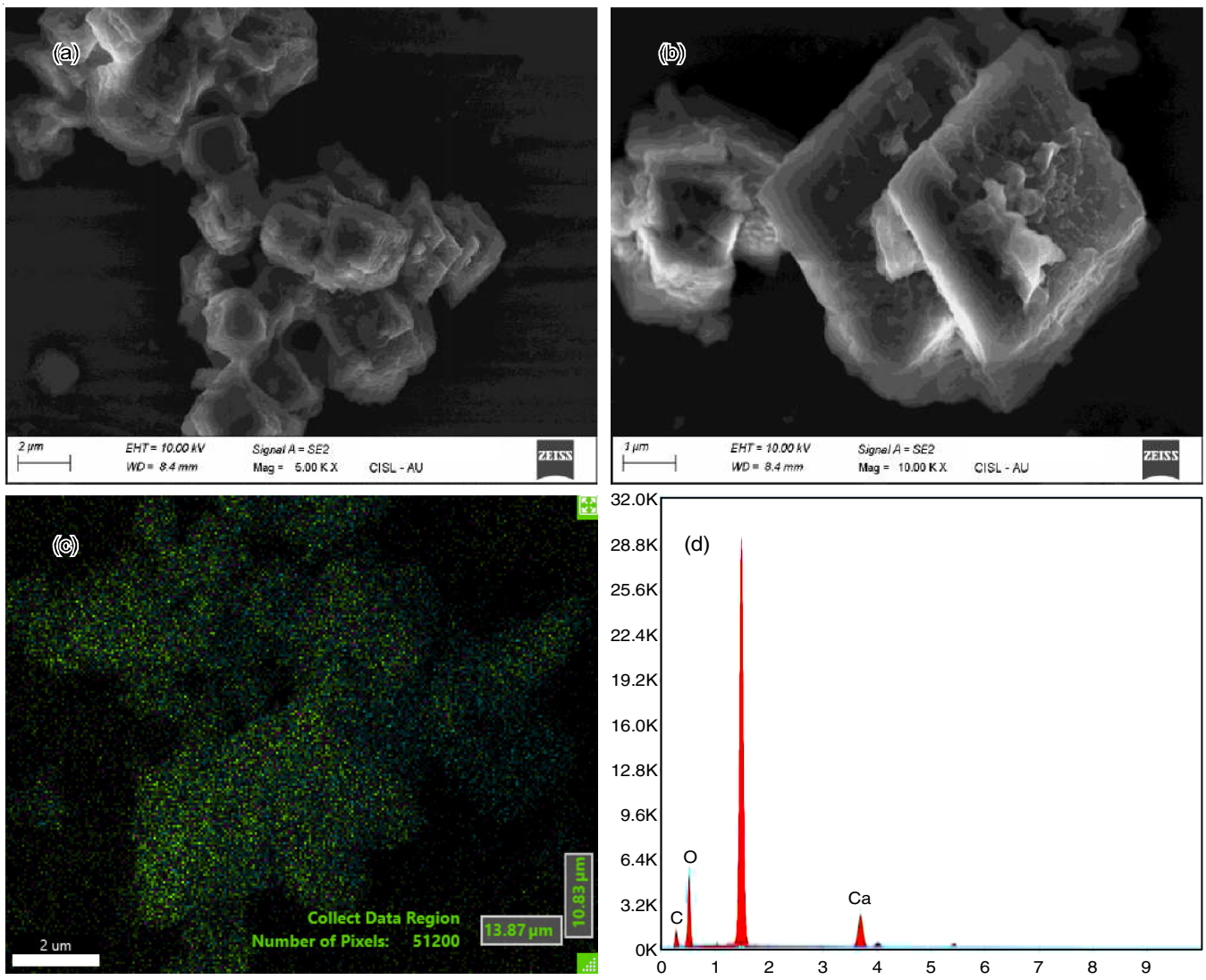

Fig. 12. (a-b) FE-SEM micrograph of pure nano $CaCO_3$ (without polymer) (c) FE-SEM elemental mapping and (d) EDX spectrum

CO_2 and the thermal dissociation of $CaCO_3$ to CaO occurs in the endothermic range of 617 and 823 ºC for pure nano $CaCO_3$ and between 464 and 832 ºC for CPN_6 nanoparticle. However, the intermediate mass loss of 6.81% from 325 ºC to 464 ºC in CPN_6 nanoparticles was due to the burning of PMMA polymer [55]. The decomposition temperature of CPN_6 nanoparticles are higher than pure nano $CaCO_3$ due to the Ni doping in the nano $CaCO_3$. When compared to previous reports, pure nano $CaCO_3$ and CPN_6 nanoparticles in the present study had greater thermal stability (823-832 ºC).

FE-SEM and EDX studies: In Fig. 12a-b, the particles are found to be accumulated as rhombohedral structures. The EDX spectrum (Fig. 12c) shows that the well-defined intense peaks for Ca, C and O as observed in pure nano $CaCO_3$. The FE-SEM images (Fig. 13a-b) show the aggregated and partially dispersed highly porous with rhombohedral shape with a rough surface in CPN_6 sample, which may be due to the influence of PMMA polymer and affords the influence on the surface of the nanoparticles [56].

Furthermore, Ca^{2+} may diffuse and aggregate due to the binding of Ca with PMMA in the formation of PMMA mediated Ca nanoparticles, which results in the increasing of calcium ion concentration. According to crystal growth kinetics, when a crystal absorbs a PMMA template on the same surface, the rate of crystal development in that direction is reduced, resulting in the isotropic growth of the crystal. Figs. 12c and 13c show the distribution of Ca, C, and O for pure nano $CaCO_3$ (without polymer) and Ca, C, O and Ni for CPN_6 nanoparticles from a chemical mapping done under a scanning electron microscope. The aforesaid findings are supported by XRD analysis.

HR-TEM studies: Figs. 14a-b and 15a-b depict the HR-TEM micrographs of pure nano $CaCO_3$ (without polymer) and CPN_6 nanoparticles, respectively. It is found that that the prepared nanoparticles were in the nanometer range and reveal the rhombohedral structure with porosity. The crystalline nature of CPN_6 (Fig. 15a) is less fibrous with more aggregation and in high magnification, which is due to the influence of doping effect. The average particle size was calculated using image J

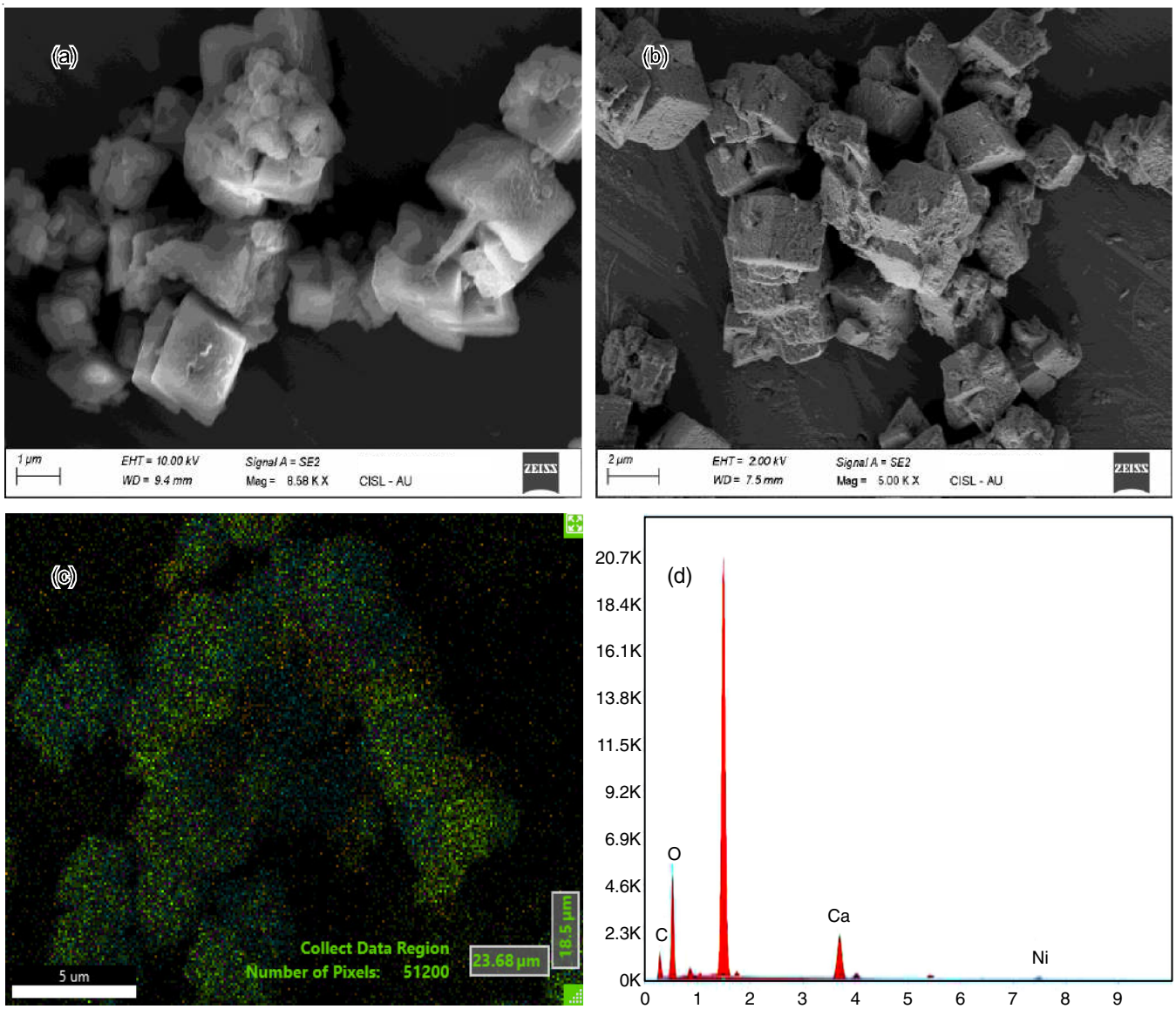

Fig. 13. (a-b) FE-SEM micrograph of CPN_6 (c) FE-SEM elemental mapping and (d) EDX spectrum

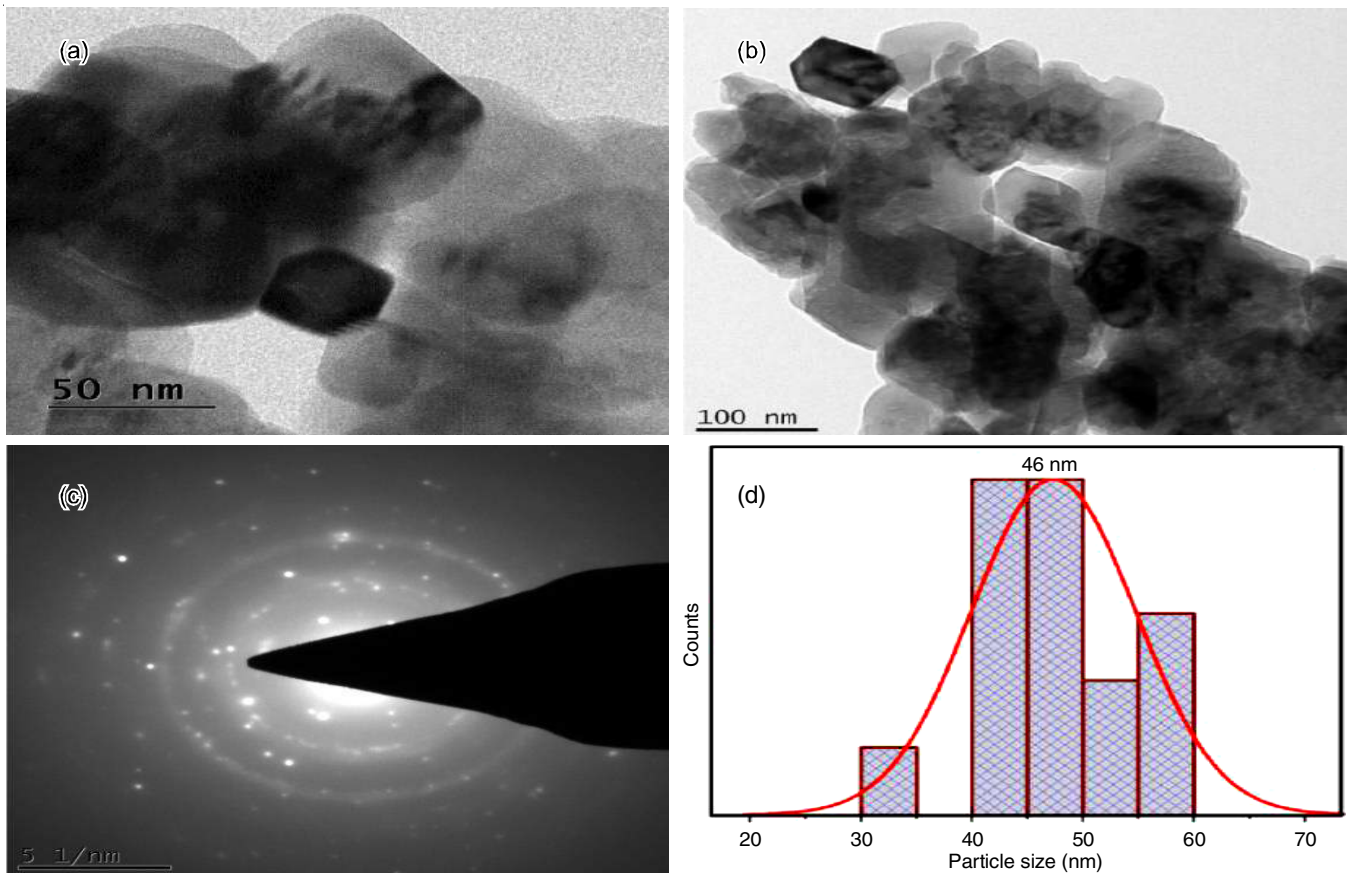

Fig. 14. (a-b) HR-TEM image of pure nano $CaCO_3$ at different magnification (b) SAED pattern and (c) particle size distribution

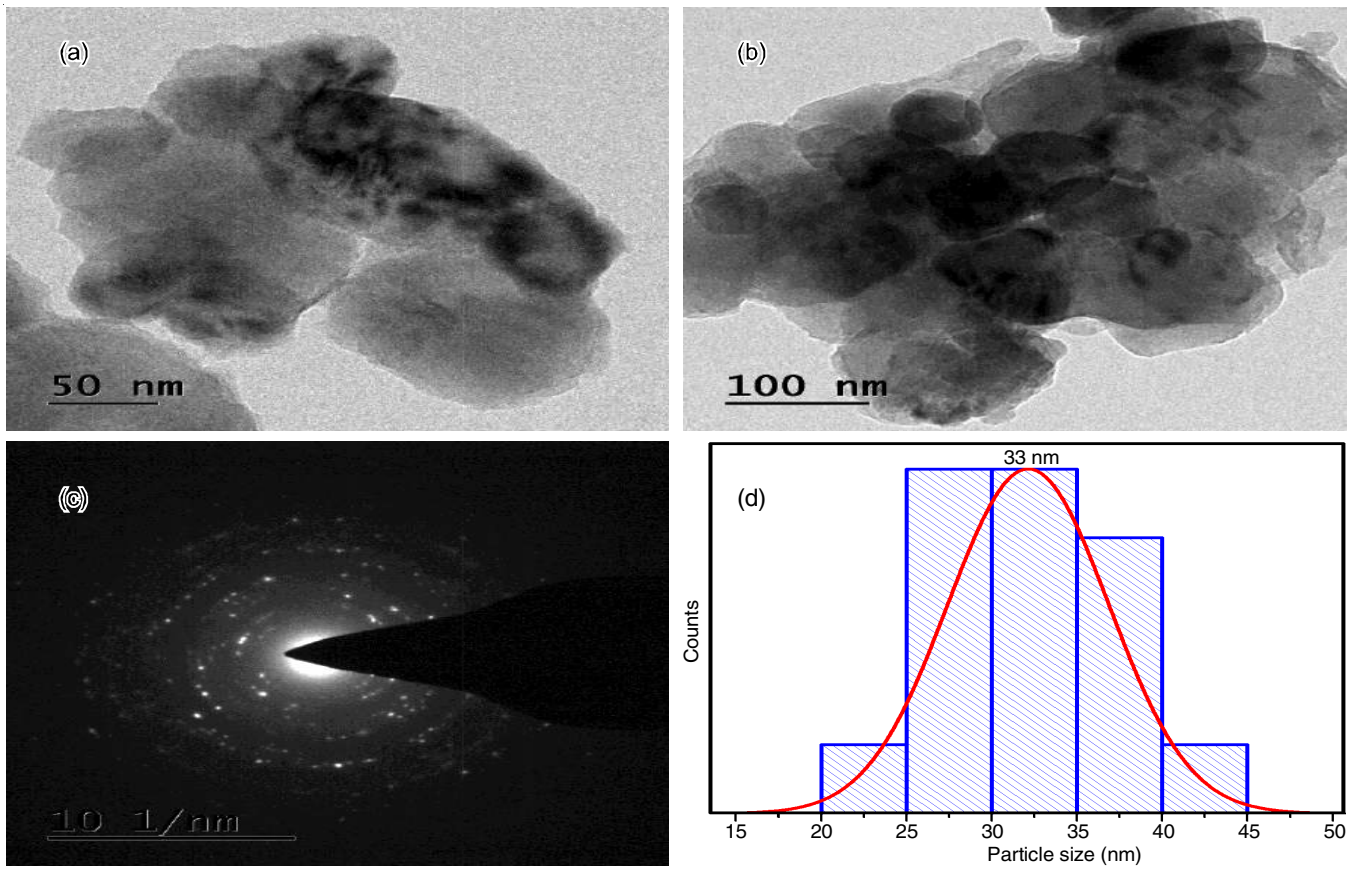

Fig. 15. (a-b) HR-TEM image of CPN_6 at different magnification (c) SAED pattern and (c) particle size distribution

1.4 package software and the corresponding size distribution diagram shown in Figs. 14d and 15d, which reveals the average domain size is about 48 and 33 nm for pure nano $CaCO_3$ and CPN_6 nanomaterial, respectively.

Figs. 14c and 15c show the SAED patterns of pure nano $CaCO_3$ and CPN_6 nanoparticles. The diffraction pattern consists of central void, which is surrounded by concentric spaced and also consist of diffused rings around it. The bright spots indicate the crystalline nature. The presences (*hkl*) planes are consistent with XRD result [57].

Photocatalytic activity: The photocatalytic activity of pure nano $CaCO_3$ (without polymer) and CPN_6 nanoparticles was examined using methylene blue and rhodamine B dyes dispersed in water under UV irradiation to migrate an electron from the valence band to the conduction band, which results in the photogeneration of electron-hole pairs. If the energy of light photons exceeds the band gap energy, the excitation of the valence band electrons will thereby promote the potential processes. In pure nano $CaCO_3$ (without polymer) and CPN_6 nanoparticles, the hole in the valence band combines with the surface H_2O molecule to produce hydroxyl radicals, which then react with the dye molecules to degrade methylene blue and rhodamine B dyes. The photodegradation efficiency (%) was calculated using eqn. 7 [58]:

$$\text{Photodegradation efficiency (\%)} = \frac{C_o - C_t}{C_o} \times 100 \quad (7)$$

where C_o is the initial concentration of dyes and C_t is the concentration of dye at irrational time.

Fig. 16a-d depicts the adsorption spectra of the photocatalytic activity of pure nano $CaCO_3$ and CPN_6 nanoparticles against methylene blue and rhodamine B dyes. It is observed that pure nano $CaCO_3$ (without polymer) and CPN_6 nanoparticles has 73% and 87% degradation for methylene blue, 88% and 97% degradation for rhodamine B dye about 2 h 30 min, respectively. The CPN_6 nanoparticles are high efficiency compare than pure nano $CaCO_3$ for both dyes. Table-2 presents the comparison data of the photocatalytic performance of nano $CaCO_3$ and CPN_6 nanoparticles in the UV irradiation.

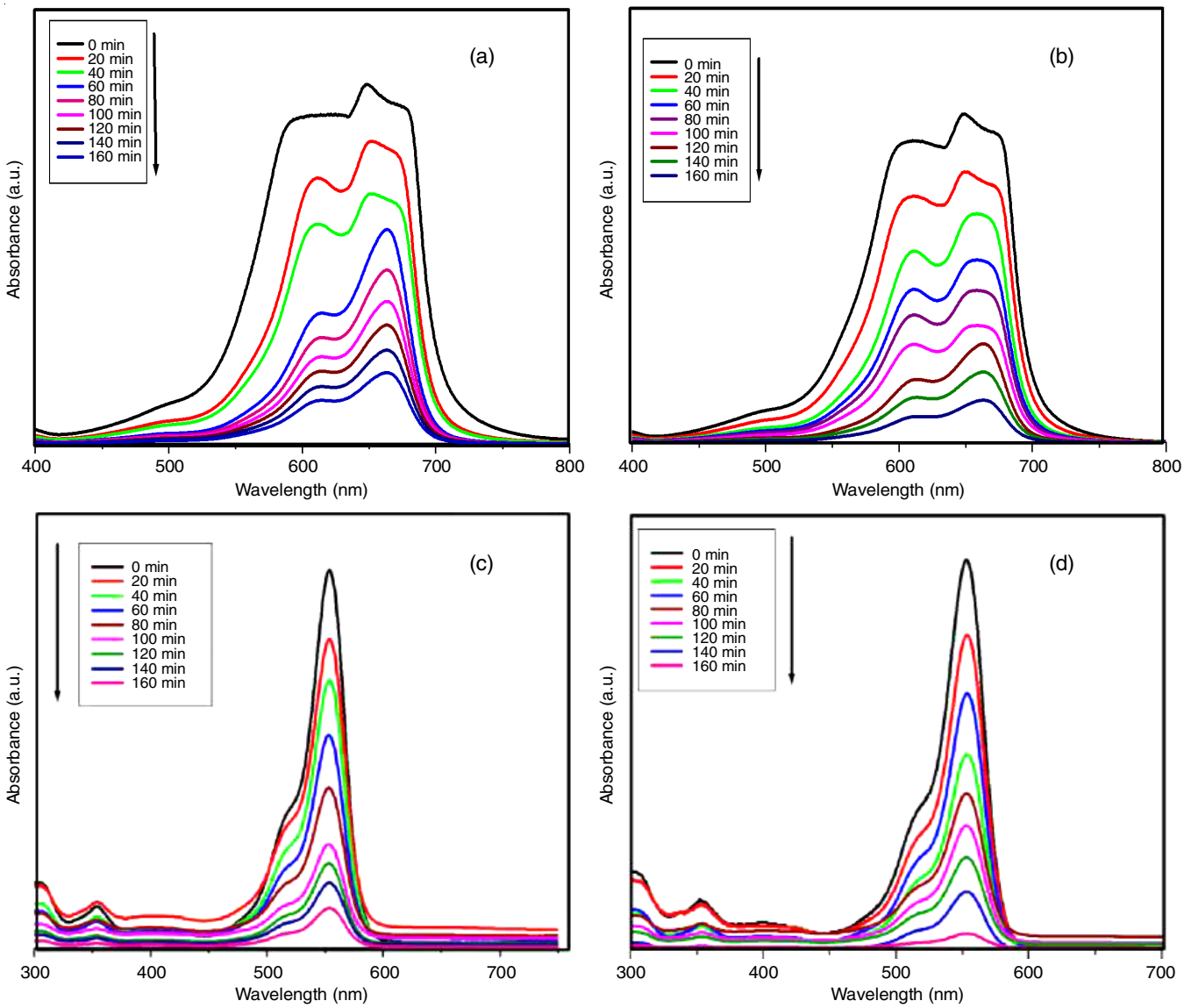

Fig. 16. Absorption spectrum of (a) pure nano $CaCO_3$ (MB), (b) CPN_6 (MB), (c) pure nano $CaCO_3$ (RhB) and (d) CPN_6 (Rh B)

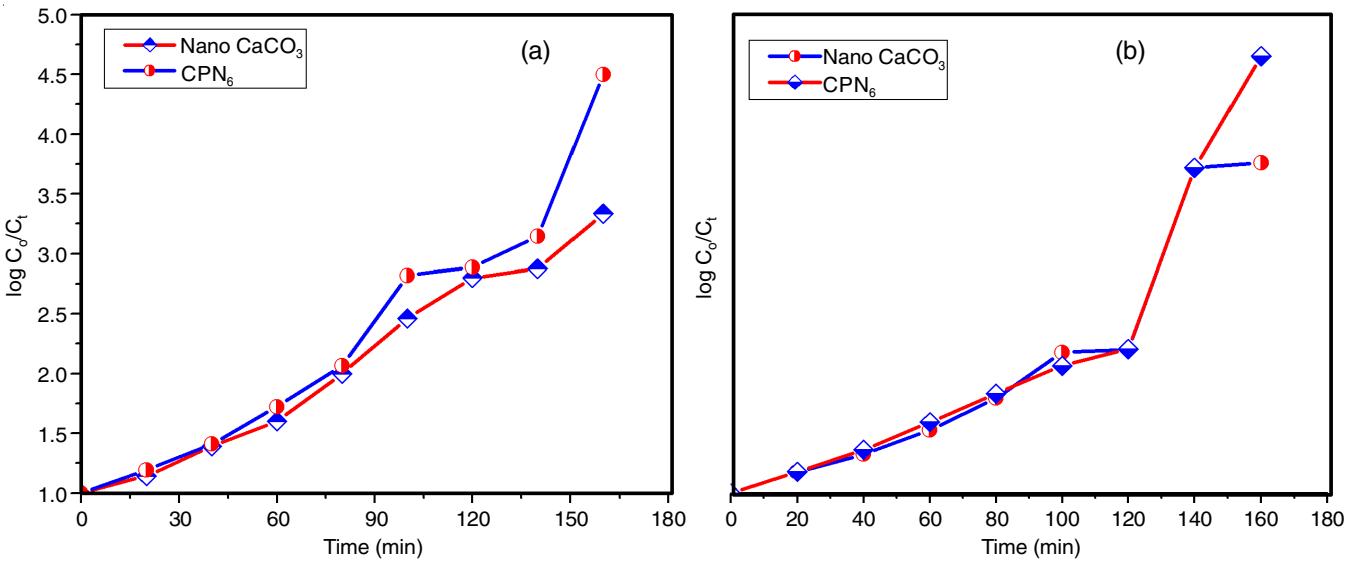

Fig. 17. Kinetic study of (a) pure nano $CaCO_3$ and CPN_6 (MB), (b) pure nano $CaCO_3$ and CPN_6 (RhB)

TABLE-2
COMPARISON OF PHOTOCATALYTIC EFFICIENCY PERCENTAGE

Photocatalyst	Reaction time (min)	Degradation (%)	Ref.
$Fe_3O_4/CaCO_3/CuWO_4$/CTAB	200	79.0	[59]
$Fe_3O_4/CaCO_3$//PEG	200	57.0	[59]
E_l//$CaCO_3$/Titania nanocomposites	120	50.0	[59]
ZnO-CeO_2 (50:50)	150	66.6	[60]
TiO_2@CNTs/AgNPs	180	68.0	[61]
Pure nano $CaCO_3$ (MB)	160	73.0	
CPN_6 (MB)	160	87.0	Present work
Pure nano $CaCO_3$ (RhB)	160	88.0	
CPN_6 (RhB)	160	97.0	

Furthermore, the pseudo-first-order kinetics model (eqn. 8) is used to obtain the rate constant values for dye degradation for the catalysts [62].

$$\ln \frac{C_o}{C_t} = K_t \quad (8)$$

where K first order rate constant at time t. Fig. 17a-b indicates the linear relationship between ln C_o/C_t and time for pure nano $CaCO_3$ (without polymer) and CPN_6 nanoparticles for methylene blue and rhodamine B dyes. From the slope of the graph, the rate constant values were calculated. The pure nano $CaCO_3$ (without polymer) and CPN_6 nanoparticles of rate constant values were 3.10×10^{-3} min^{-1} and 4.07×10^{-3} min^{-1}, 3.35×10^{-3} min^{-1} and 4.53×10^{-3} min^{-1} in methylene blue and rhodamine B dyes, respectively.

Effect of scavengers: The reactive species of $^{\bullet}O_2^-$, h^+, superoxide radicals and $^{\bullet}OH$ are often recognized as the major species that may react with organic contaminants and break them down into smaller fragments in the heterogeneous photocatalytic processes. To clarify the significance function of these species, $AgNO_3$ (Ag^+), isopropanol acid (IPA), EDTA2Na and ascorbic acid (AA) were used as electron (e^-), hydroxyl radicals (OH), holes (h^+) and superoxide ion radicals ($^{\bullet}O_2^-$) scavengers, respectively. The results show that when scavenging agents such as Ag^+, EDTA2Na and IPA were added, the degree of photodegradation by CPN_6 sample was less than when no scavenger was present. In absence of any scavengers, the photocatalyst degrade 97% of rhodamine B dye molecules, but in the presence of 1 mM Ag(I), EDTA2Na, IPA and AA, these percentages fell to 12%, 23%, 17% and 9%, respectively (Fig. 18).

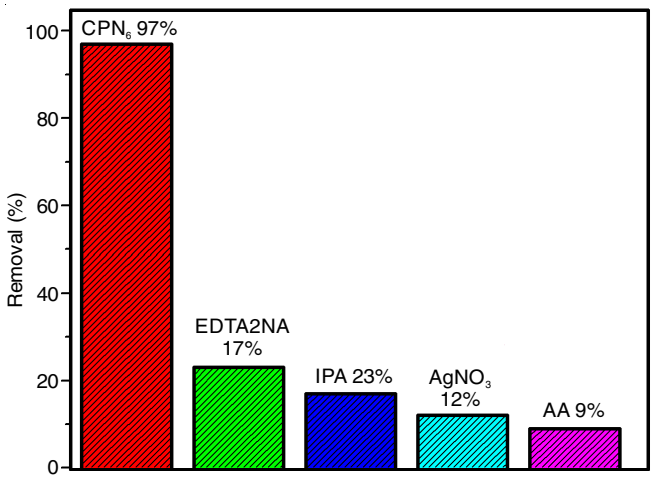

Fig. 18. Effect of scavengers for CPN_6 in rhodamine B dye

The scavengers for the photogenerated electrons are known as Ag^+ cations. Because the e^-/h^+ recombination process is reduced, the photogenerated hole has a greater opportunity to interact with water and generate more hydroxyl radicals [63]. In different mechanism, the interaction of silver cations with photogenerated electrons may result in the formation of a silver cluster on the surface of composite, some of which may function as an electron sink. Superoxide radicals can be created when the gathered electrons in sink interact with the dissolved oxygen. When these clusters are larger and more numerous and may serve as bulk silver sites for the e^-/h^+ recombination ($e^- + Ag^+ \rightarrow {}^{\bullet}Ag$, $^{\bullet}Ag. + Ag^+ + e^- \rightarrow Ag_n$). Consequently, the

ideal size of a hole scavenger called EDTA2Na produces anion radicals, which are less active than OH radicals [64]. According to the findings, the order of AA > $AgNO_3$ > IPA > EDTA2Na indicates the degree of inhibition. This pattern supports the critical roles played by photogenerated electrons and holes, as well as hydroxyl radicals, in the photocatalytic degradation of rhodamine B dye by CPN_6 sample.

Photocatalytic mechanism: Photocatalytic process for the breakdown of methylene blue and rhodamine B dyes over $CaCO_3$ and Ni doped $CaCO_3$ nanoparticles using UV light irradiation is shown in Fig. 19. When $CaCO_3$ absorbs photons with energy, which is equivalent to or higher than its band gap energy, an electron may be driven from the valance band (VB) of $CaCO_3$ to the conduction band (CB) of $CaCO_3$ and simultaneously, a vacancy or "hole" may be left in the VB of $CaCO_3$. This is possible because $CaCO_3$ has band gap energy. In the process of tailoring $CaCO_3$ by adding Ni, the electron with the highest energy content in the CB may contained Ni, which acts as an electron trap and effectively distinguishes the production of (e^-/h^+) pairs. Nickel has electrons and when coupled with oxygen, generate superoxide. As a result, the hole in the VB of Ni-doped $CaCO_3$ will undergo charge transfer to the hydroxyl group adsorbed on the surface of catalyst, resulting in the formation of hydroxyl radicals [65]. The hydroxyl radicals react with the dye molecules during the photocatalytic, which ultimately results in the effective destruction of the dye molecules. In present case, the super oxide radicals were found to be the predominant species produced in the Ni-doped $CaCO_3$.

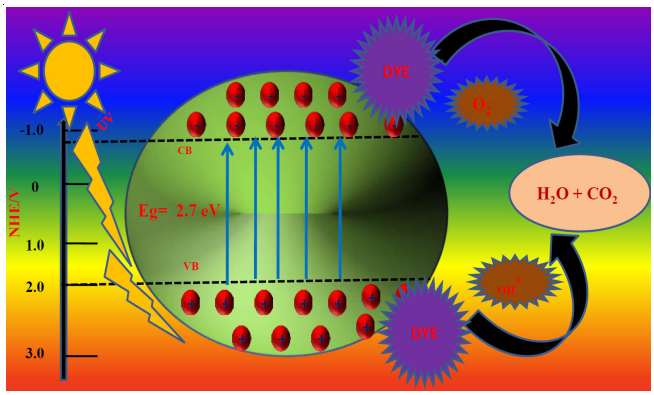

Fig. 19. Possible photocatalytic mechanism of CPN_6 nanoparticles

Conclusion

The nano $CaCO_3$ and PMMA mediated Ni-doped $CaCO_3$ nanoparticles (CPN_6) were successfully synthesized through a biomimetic synthetic route and systematically characterized using sophisticated techniques. The increased crystallite size and optical properties of the CPN_6 nanoparticles was support the enhancement of degradation efficiency against methylene blue and rhodamine B dyes. Further, various scavengers were used to examine the efficiency of photocatalytic performance of the product, which resulted the super oxide scavenger (ascorbic acid) play a vital role while the hole scavenger (EDTA ·2Na) also plays a minor role in the efficiency of the product. Using the UV-visible light irradiation, sample CPN_6 achieved 87% and 97% dye degradation efficiency against methylene blue and rhodamine B dyes respectively after 160 min.

CONFLICT OF INTEREST

The authors declare that there is no conflict of interests regarding the publication of this article.

REFERENCES

1. C. He, Z. Liu, J. Wu, X. Pan, Z. Fang, J. Li and B.A. Bryan, *Nat. Commun.*, **12**, 4667 (2021); https://doi.org/10.1038/s41467-021-25026-3
2. P.H. Gleick, *Water Int.*, **25**, 127 (2000); https://doi.org/10.1080/02508060008686804
3. S.B. Moore and L.W. Ausley, *J. Clean. Prod.*, **12**, 585 (2004); https://doi.org/10.1016/S0959-6526(03)00058-1
4. X. Zhang, Y. Pan, J. Zhao, X. Hao, Y. Wang, D.W. Schubert, C. Liu, C. Shen, X. Liu, *Eng. Sci.*, **7**, 65 (2019); https://doi.org/10.30919/es8d505
5. K. Rani, J. Singh, A. Jangra, P. Kumar, S. Kumar and R. Kumar, *Asian J. Chem.*, **34**, 619 (2022); https://doi.org/10.14233/ajchem.2022.23532
6. A.R. Khataee and M.B. Kasiri, *J. Mol. Catal. Chem.*, **328**, 8 (2010); https://doi.org/10.1016/j.molcata.2010.05.023
7. T.C. dos Santos, G.J. Zocolo, D.A. Morales, G.A. Umbuzeiro and M.V.B. Zanoni, *Food Chem. Toxicol.*, **68**, 307 (2014); https://doi.org/10.1016/j.fct.2014.03.025
8. P. Nigam, G. Armour, I.M. Banat, D. Singh and R. Marchant, *Bioresour. Technol.*, **72**, 219 (2000); https://doi.org/10.1016/S0960-8524(99)00123-6
9. E.J. Weber and R.L. Adams, *Environ. Sci. Technol.*, **29**, 1163 (1995); https://doi.org/10.1021/es00005a005
10. J.L. Adrio and A.L. Demain, *Biomolecules*, **4**, 117 (2014); https://doi.org/10.3390/biom4010117
11. M.S. Lucas, A.A. Dias, A. Sampaio, C. Amaral and J.A. Peres, *Water Res.*, **41**, 1103 (2007); https://doi.org/10.1016/j.watres.2006.12.013
12. S. Dong, J. Feng, M. Fan, Y. Pi, L. Hu, X. Han, M. Liu, J. Sun and J. Sun, *RSC Adv.*, **5**, 14610 (2015); https://doi.org/10.1039/C4RA13734E
13. S. Zhu and D. Wang, *Adv. Energy Mater.*, **7**, 1700841 (2017); https://doi.org/10.1002/aenm.201700841
14. W.S. Koe, J.W. Lee, W.C. Chong, Y.L. Pang and L.C. Sim, *Environ. Sci. Pollut. Res. Int.*, **27**, 2522 (2020); https://doi.org/10.1007/s11356-019-07193-5
15. S. Rong, X. Tang, H. Liu, J. Xu, Z. Yuan, X. Peng, J. Niu, Y. Wu, L. He and K. Qian, *NanoImpact*, **22**, 100304 (2021); https://doi.org/10.1016/j.impact.2021.100304
16. S.K. Loeb, P.J.J. Alvarez, J.A. Brame, E.L. Cates, W. Choi, J. Crittenden, D.D. Dionysiou, Q. Li, G. Li-Puma, X. Quan, D.L. Sedlak, T.D. Waite, P. Westerhoff and J.-H. Kim, *Environ. Sci. Technol.*, **53**, 2937 (2019); https://doi.org/10.1021/acs.est.8b05041
17. S. Sharma and A. Bhattacharya, *Appl. Water Sci.*, **7**, 1043 (2017); https://doi.org/10.1007/s13201-016-0455-7
18. S. Peiris, J. McMurtrie and H.Y. Zhu, *Catal. Sci. Technol.*, **6**, 320 (2016); https://doi.org/10.1039/C5CY02048D
19. K.K. Jaiswal, S. Dutta, C.B. Pohrmen, R. Verma, A. Kumar and A.P. Ramaswamy, *Inorg. Nan-Met. Chem.*, **51**, 995 (2021); https://doi.org/10.1080/24701556.2020.1813769
20. Z.S. Zhu, X.J. Yu, J. Qu, Y.Q. Jing, Y. Abdelkrim and Z.Z. Yu, *Appl. Catal. B*, **261**, 118238 (2020); https://doi.org/10.1016/j.apcatb.2019.118238
21. Y. Liu, X. He, X. Duan, Y. Fu, D. Fatta-Kassinos and D.D. Dionysiou, *Water Res.*, **95**, 195 (2016); https://doi.org/10.1016/j.watres.2016.03.011
22. J.A. McKenzie and C. Vasconcelos, *Sedimentology*, **56**, 205 (2009); https://doi.org/10.1111/j.1365-3091.2008.01027.x
23. X. Zhang, M. Liu, Z. Kang, B. Wang, B. Wang, F. Jiang, X. Wang, D.-P. Yang and R. Luque, *Chem. Eng. J.*, **388**, 124304 (2020); https://doi.org/10.1016/j.cej.2020.124304

24. T.B.N.S. Madugalla, H.M.T.G.A. Pitawala and D.G.G.P. Karunaratne, *Nat. Resour. Res.*, **23**, 217 (2014); https://doi.org/10.1007/s11053-013-9222-8
25. S. Singh, H. Mahalingam and P.K. Singh, *Appl. Catal. A Gen.*, **462-463**, 178 (2013); https://doi.org/10.1016/j.apcata.2013.04.039
26. J. Lv, L. Qiu and B. Qu, *J. Cryst. Growth*, **267**, 676 (2004); https://doi.org/10.1016/j.jcrysgro.2004.04.034
27. V. Melinte, L. Stroea and A.L. Chibac-Scutaru, *Catalysts*, **9**, 986 (2019); https://doi.org/10.3390/catal9120986
28. C. Yang, X. Wang, Y. Ji, T. Ma, F. Zhang, Y. Wang, M. Ci, D. Chen, A. Jiang and W. Wang, *NanoImpact*, **15**, 100174 (2019); https://doi.org/10.1016/j.impact.2019.100174
29. R. Gusain, K. Gupta, P. Joshi and O.P. Khatri, *Adv. Colloid Interface Sci.*, **272**, 102009 (2019); https://doi.org/10.1016/j.cis.2019.102009
30. C. Karthikeyan, P. Arunachalam, K. Ramachandran, A.M. Al-Mayouf and S. Karuppuchamy, *J. Alloys Compd.*, **828**, 154281 (2020); https://doi.org/10.1016/j.jallcom.2020.154281
31. M.M. Nassar, T.E. Farrag, M.S. Mahmoud, S. Abdelmonem, K.A. Khalil and N.A.M. Barakat, *Adv. Powder Technol.*, **26**, 914 (2015); https://doi.org/10.1016/j.apt.2015.03.006
32. M.A. Karimi and M. Ranjbar, *Synth. React. Inorg. Met.-Org. Nano-Met. Chem.*, **46**, 635 (2016); https://doi.org/10.1080/15533174.2014.988817
33. Q. Cheng, M. Kang, J. Wang, P. Zhang, R. Sun and L. Song, *Adv. Powder Technol.*, **26**, 848 (2015); https://doi.org/10.1016/j.apt.2015.02.010
34. A.K. Sugih, D. Shukla, H.J. Heeres and A. Mehra, *Nanotechnology*, **18**, 035607 (2007); https://doi.org/10.1088/0957-4484/18/3/035607
35. T. Tsuzuki, K. Pethick and P.G. McCormick, *J. Nanopart. Res.*, **2**, 375 (2000); https://doi.org/10.1023/A:1010051506232
36. M. Gaft, L. Nagli, G. Panczer, G. Waychunas and N. Porat, *Am. Mineral.*, **93**, 158 (2008); https://doi.org/10.2138/am.2008.2576
37. V. Ramasamy, P. Anand and G. Suresh, *Adv. Powder Technol.*, **29**, 818 (2018); https://doi.org/10.1016/j.apt.2017.12.023
38. D. Zhang, *Russ. J. Phys. Chem. A. Focus Chem.*, **86**, 93 (2012); https://doi.org/10.1134/S0036024412010086
39. V. Ramaswamy, V. Ponnusamy and J. Hemalatha, *Indian J. Phys.*, **79**, 847 (2005).
40. H.M. Zidan and M. Abu-Elnader, *Physica B*, **355**, 308 (2005); https://doi.org/10.1016/j.physb.2004.11.023
41. A. Shafiu Kamba, M. Ismail, T.A. Tengku Ibrahim and Z.A.B. Zakaria, *J. Nanomater.*, **2013**, 398357 (2013); https://doi.org/10.1155/2013/398357
42. L. Vaculikova and E. Plevova, *Acta Geodyn. Geomater.*, **2**, 163 (2005).
43. M.K. Pal, B. Singh and J. Gautam, *J. Therm. Anal. Calorim.*, **107**, 85 (2012); https://doi.org/10.1007/s10973-011-1686-3
44. X. Ma, B. Zhou, Y. Deng, Y. Sheng, C. Wang, Y. Pan and Z. Wang, *Colloids Surf. A Physicochem. Eng. Asp.*, **312**, 190 (2008); https://doi.org/10.1016/j.colsurfa.2007.06.058
45. S. Sivakumar, N.A. Mala, K.M. Batoo and E.H. Raslan, *Mater. Technol.*, **37**, 1375 (2022); https://doi.org/10.1080/10667857.2021.1949527
46. M.M.M.G.P.G. Mantilaka, D.G.G.P. Karunaratne, R.M.G. Rajapakse and H.M.T.G.A. Pitawala, *Powder Technol.*, **235**, 628 (2013); https://doi.org/10.1016/j.powtec.2012.10.048
47. M. Ahamed, M.A. Khan, M.J. Akhtar, H.A. Alhadlaq and A. Alshamsan, *Sci. Rep.*, **6**, 30196 (2016); https://doi.org/10.1038/srep30196
48. L. Wu, J.A. Aguiar, P.P. Dholabhai, T. Holesinger, B.P. Uberuaga, T. Aoki and R.H. Castro, *J. Phys. Chem. C*, **119**, 27855 (2015); https://doi.org/10.1021/acs.jpcc.5b09255
49. S. Dutta, S. Som and S.K. Sharma, *Dalton Trans.*, **42**, 9654 (2013); https://doi.org/10.1039/c3dt50780g
50. V. Ramasamy and G. Vijayalakshmi, *J. Mater. Sci. Mater. Electron.*, **27**, 4723 (2016); https://doi.org/10.1007/s10854-016-4352-5
51. J.R. Weertman, *Mater. Sci. Eng. A*, **166**, 161 (1993); https://doi.org/10.1016/0921-5093(93)90319-A
52. H. Van Swygenhoven, *Science*, **296**, 66 (2002); https://doi.org/10.1126/science.1071040
53. M. Samtani, D. Dollimore, F.W. Wilburn and K. Alexander, *Thermochim. Acta*, **367-368**, 285 (2001); https://doi.org/10.1016/S0040-6031(00)00662-6
54. A.S. Kamba, M. Ismail, T.A.T. Ibrahim and Z.A.B. Zakaria, *J. Nanomater.*, **2017**, 398357 (2017); https://doi.org/10.1155/2013/398357
55. M.R. Abeywardena, R.K.W.H.M.K. Elkaduwe, D.G.G.P. Karunarathne, H.M.T.G.A. Pitawala, R.M.G. Rajapakse, A. Manipura and M.M.M.G.P.G. Mantilaka, *Adv. Powder Technol.*, **31**, 269 (2020); https://doi.org/10.1016/j.apt.2019.10.018
56. A. Chatterjee and S. Mishra, *Particuology*, **11**, 760 (2013); https://doi.org/10.1016/j.partic.2012.11.005
57. M. Nakayama, S. Kajiyama, T. Nishimura and T. Kato, *Chem. Sci.*, **6**, 6230 (2015); https://doi.org/10.1039/C5SC01820J
58. Y. Liu, Y. Jiang, M. Hu, S. Li and Q. Zhai, *Chem. Eng. J.*, **273**, 371 (2015); https://doi.org/10.1016/j.cej.2015.03.109
59. E.M.S. Azzam, N.A. Fathy, S.M. El-Khouly and R.M. Sami, *J. Water Process Eng.*, **28**, 311 (2019); https://doi.org/10.1016/j.jwpe.2019.02.016
60. W. Lin, B. Xu and L. Liu, *New J. Chem.*, **38**, 5509 (2014); https://doi.org/10.1039/C4NJ01251H
61. A.E. Wagner, P. Huebbe, T. Konishi, M.M. Rahman, M. Nakahara, S. Matsugo and G. Rimbach, *J. Agric. Food Chem.*, **56**, 11694 (2008); https://doi.org/10.1021/jf802403d
62. M.J. Enayat, *J. Mater. Sci. Mater. Electron.*, **29**, 19435 (2018); https://doi.org/10.1007/s10854-018-0072-3
63. K. Villa, S. Murcia-López, T. Andreu and J.R. Morante, *Appl. Catal. B*, **163**, 150 (2015); https://doi.org/10.1016/j.apcatb.2014.07.055
64. T. Tan, D. Beydoun and R. Amal, *J. Photochem. Photobiol. Chem.*, **159**, 273 (2003); https://doi.org/10.1016/S1010-6030(03)00171-0
65. J.C. Sin, S.M. Lam, K.T. Lee and A.R. Mohamed, *Ceram. Int.*, **40**, 5431 (2014); https://doi.org/10.1016/j.ceramint.2013.10.128